




The Impact of Ni- and Cr-Containing Thermally Grown Oxides on the Intensity of Oxide and Sulfate Induced Hot Corrosion of an Alumina-Forming Alloy

ATHARVA S. CHIKHALIKAR¹ and DAVID L. POERSCHKE ^{1,2}

1.—Department of Chemical Engineering and Material Science, University of Minnesota Twin Cities, Minneapolis, MN 55455, USA. 2.—e-mail: poerschke@umn.edu

Aerosols deposited on the surfaces of alloys and coatings used in high-temperature applications react with the protective thermally grown oxide (TGO) and accelerate component degradation. Understanding how the TGO composition effects these reactions is essential to develop corrosion-resistant materials. This work studies the corrosion of Haynes-214 alloy, which forms a bilayer Ni(Cr,Al)₂O₄ (spinel) + Al₂O₃ TGO, exposed to complex oxide and sulfate deposits to understand how the Cr and Ni oxides affect the corrosion mechanisms. The deposit compositions were systematically varied to understand the effect of anion makeup (mixed oxides, oxide-sulfate, and sulfates). The results are compared to a FeCrAlY alloy that forms a simple Al₂O₃ TGO. On the Haynes-214 alloy, deposits containing mixed oxides (with or without sulfates) have limited corrosive effect. In contrast, a pure CaSO₄ deposit reacts aggressively with the TGO to form calcium chromate and aluminate reaction products (RP) that substantially increase the TGO + RP thickness compared to that on the FeCrAlY alloy. Surprisingly, a deposit composed of a mixture of sulfates caused less severe corrosion than the CaSO₄ alone since magnesium chromate formation appears to limit aggressive reactions involving Ca. The results are discussed in the context of opportunities for corrosion-resistant alloy design.

INTRODUCTION

The alloys and metallic coatings utilized in aerospace, marine, and land-based turbines are protected against oxidative atmospheres at high temperatures by forming a dense, adherent thermally grown oxide (TGO).^{1,2} The protection afforded by the TGO can be degraded when aerosols (such as salts, ashes, dust, etc.) are ingested and subsequently deposited onto component surfaces. Species in these deposits can react with the TGO or the alloy components forming reaction products that disrupt the TGO and ultimately accelerate the oxidative degradation of the alloys. The alloy composition, which determines the TGO composition, structure, and ability to re-passivate after the TGO is

disrupted, affects the reactions with the deposits and is an important parameter to consider while studying deposit-induced hot corrosion mechanisms to enable the design of more durable alloys.

Most prior work on deposit-induced degradation of alloys has focused on temperatures < 950°C where Na₂SO₄ is the primary corrodent.^{3–14} That work identified important effects of alloying elements, such as the fact that molybdenum (Mo) and tungsten (W) increase the corrosion intensity by altering the fluxing mechanisms^{3,15–17} while chromium (Cr) can mitigate corrosion.^{9,18,19} The examination of ex-service turbine components in conjunction with the laboratory experiments indicates that, at higher temperatures, deposits with more complex chemistry (such as multi-cation sulfate, sulfate-oxide, and sulfate-oxide-chloride mixtures) accelerate oxidation via a variety of mechanisms.^{20–28} Related work showed that CaO- and CaSO₄ in such deposits are particularly

(Received January 22, 2024; accepted April 15, 2024; published online May 28, 2024)

important corrodents that convert the protective TGO into less protective calcium-aluminate and -chromate products* and can initiate alloy sulfidation.^{16,32,34–37} Studies performed on the Ca-based corrosion of β - and γ -phase NiCoCrAlY show that the composition and fraction of β (Al-rich) and γ (Cr-rich) phases affect the degradation intensity. Specifically, single-phase β alloys performed best, while the Cr-rich γ promotes forming calcium chromate on reaction with CaO that reduces the ability of the alloy to re-passivate by the formation of a thin alumina layer.³² That work suggests that increasing the Cr content has a detrimental effect due to the formation of low-melting temperature chromate species. Gheno and Gleason also observed that γ -rich NiCoCrAlY bond coats are susceptible to internal oxidation and nitridation in the presence of mixed oxide and mixed oxide + Na₂SO₄ type of deposits.²⁰

Understanding how the interplay among the oxidation conditions (temperature, atmosphere), the alloy and TGO composition, and the deposit constitution influences the corrosion intensity is critical to the development of next-generation corrosion-resistant alloys. Our prior investigation of the effect of multi-component deposit composition on the corrosion of alumina-forming alloy demonstrated that while the sulfates attack the TGO and form aluminate reaction products, deposits based on mixtures of oxides or oxides and sulfates produced limited, localized attack.^{38,39} The difference between the behavior of oxide-sulfate and the sulfate deposits was attributed to reactions with the oxides that accelerated sulfate decomposition and lowered the calcium activity by forming Ca-containing aluminosilicates.^{38,40} It was also observed that while Na₂SO₄ in the multi-cation mixed sulfate deposit fluxed the deposit, the underlying TGO-deposit reactions formed products that were similar to the specimen exposed to CaSO₄ alone.

There are many open questions about how Ni and Cr affect the corrosion mechanisms for alloys exposed to complex deposit chemistries. In particular, this study focuses on the following questions:

- Do Ca-containing deposits based on mixtures of oxides or sulfates react with the TGO to form calcium chromates to the same extent as pure CaSO₄ deposits?
- Can reactions caused by a complex deposit

chemistry disrupt a pre-existing TGO? If so, how severe is the attack on the exposed alloy?

- How different are the deposit-induced degradation products or reaction pathways for an alloy that forms a TGO containing Ni and Cr oxides in addition to alumina compared to an alloy that forms a pure alumina TGO? Are these products different for deposits containing mixtures of oxide, oxides, and sulfates or just sulfates?

To address these questions, we analyzed the oxidation behavior of Haynes-214 alloy, a Ni-based superalloy that forms a dual-layered (Ni(Cr,Al)₂O₄ + Al₂O₃) TGO, in the presence of deposits comprising mixtures of oxides, oxides with sulfates, and mixed sulfates. Image analysis was used to quantify features including the reaction product thickness and the alloy/TGO interface roughness. These results are compared to prior work on an Al₂O₃-forming FeCrAlY alloy. The work offers new insights into the role of TGO composition and structure on alloy degradation while also generating datasets for future data-driven materials discovery efforts.

APPROACH AND METHODS

Deposit Selection and Preparation

Table I lists the six deposit compositions studied; the rationale for selecting these compositions and details of the synthesis approach are provided elsewhere.^{39,40} In brief, the compositions are derived from a master cation stoichiometry C₁₃N₁₀K₁M₁₁F₁₁A₁₄S₄₀ with varied anion makeup including mixed sulfates ($-\bar{S}$), mixed oxides ($-O$), or mixed oxides and sulfates ($-O\bar{S}$). Variants were also tested with and without the more volatile and lower melting Na and K components. The oxide-sulfate mixtures are formulated with Ca, Mg, Na, and K added in a 1:2 sulfate-to-oxide ratio, whereas the other cations (Fe, Al, and Si) were added only as oxides since their sulfates are not stable under the relevant conditions.^{41–43} The mixed sulfate CNKM $-\bar{S}$ was formulated with just the sulfate-forming cations (Ca, Na, K, and Mg) in the same ratios as the master stoichiometry. The deposits were synthesized from individual oxide and sulfate components, > 99% pure, procured from either Alfa Aesar (Ward Hill, MA) or Acros Organics (Morris Hill, NJ) using a sequential mixing and heat treatment approach to facilitate pre-reaction between the oxide components without decomposing the sulfates.

Oxidation Testing

Tests were conducted on Haynes-214 alloy (Ni(bal.)-16Cr-4.5Al-3Fe-2Co, wt.%) (Haynes International, IN). When oxidized in a clean environment at temperatures > 850°C, this alloy forms a dual-layered TGO with an inner α -Al₂O₃ layer and outer

*There are multiple intermediate compounds in both the Al₂O₃-CaO and CaO-Cr₂O₃ systems.^{29–33} Reaction products formed during alloy oxidation under Ca-containing deposits often contain aluminate or chromate compounds that are not always easily distinguishable. Furthermore, there are some inconsistencies in the reported equilibrium phases in the CaO-Cr₂O₃ system.^{32,33} We adopt the nomenclature Ca_xAl_yO_z and Ca_xCr_yO_z to refer generically to calcium-aluminate and -chromate reaction products.

Table I. Summary of deposit compositions (mol.%)*

ID and cation stoichiometry ↓ Component	C ₁₅ M ₁₂ F ₁₂ A ₁₆ S ₄₅		C ₁₃ N ₁₀ K ₁ M ₁₁ F ₁₁ A ₁₄ S ₄₀		C ₃₇ N ₂₈ K ₃ M ₃₁	C ₁₀₀
	CMFAS-O	CMFAS-O \bar{S}	CNKMFAS-O	CNKMFAS-O \bar{S}	CNKM- \bar{S}	CaSO ₄
AlO _{1.5}	16	16	14	14	–	–
CaO	15	10	13	9	–	–
FeO _{1.5}	12	12	11	11	–	–
KO _{0.5}	–	–	1	0.7	–	–
MgO	12	8	11	7	–	–
NaO _{0.5}	–	–	10	7	–	–
SiO ₂	45	45	40	40	–	–
CaSO ₄	–	5	–	5	37	100
K(SO ₄) _{0.5}	–	–	–	0.3	3	–
MgSO ₄	–	4	–	4	28	–
Na(SO ₄) _{0.5}	–	–	–	3	31	–

*Single cation cement chemistry notation C = CaO, N = NaO_{0.5}, A = AlO_{1.5}, S = SiO₂, \bar{S} = SO₃, etc. Adapted from Ref.38.

Ni(Cr,Al)₂O₄ spinel layer.^{44,45} Coupons, approximately 12 mm long and 8 mm wide, were cut from a 1.75-mm-thick plate by wire EDM. The surfaces were polished using SiC abrasive papers and diamond polishing suspensions to a 1 μ m diamond finish and then ultrasonically cleaned sequentially in a 2 wt.% microorganic soap solution, 200 proof ethanol, and acetone. The specimens were measured and weighed before and after each heat treatment. Before the deposit-induced degradation experiments, each specimen was pre-oxidized for 100 h in dry air (< 6 ppm H₂O, 0.2 l/min, 30 mm OD, 27 mm ID fused quartz tube) at 1025°C (10°C/min heating, 8°C/min maximum cooling rate).

The powdered deposits were applied on a portion of the specimen using a stencil to achieve a \sim 25 mg/cm² loading over a \sim 4-mm-diameter circle. After application, the deposit powder was lightly compacted against the specimen surface using a cylindrical steel punch to improve contact. Then, the specimens with the deposit were placed in alumina boats (Coorstek Inc., Golden, CO) and annealed for an additional 100 h at 1025°C in dry air using the same conditions as the pre-oxidation. To avoid cross-contamination, separate furnace tubes and boats were utilized for each deposit type. A baseline sample was generated by heat-treating the alloy under the same conditions without a deposit.

Characterization

The specimen surfaces were visually inspected to determine the degree of deposit adherence, melting, and spreading. Photo-stimulated luminescence spectroscopy (PSLS) and Raman spectroscopy techniques were used to confirm the presence of α -Al₂O₃ and Ni(Cr,Al)₂O₄ spinel, respectively, in the TGO using a 532-nm Nd:YAG laser on the Witec Alpha 300R confocal Raman microscope. Polished cross

sections were characterized by scanning electron microscopy (SEM, Hitachi SU8230) and energy dispersive x-ray spectroscopy (EDS, Thermo-Noran Vantage on a JEOL JSM 6500 SEM). The specimens were cut, ground, and polished using water-free lubricants to prevent loss of water-soluble deposits and reaction products. Back-scattered electron (BSE) micrographs were recorded across the entire cross section at a sufficiently high magnification to identify details of the TGO and TGO-alloy interface. These BSE images were merged and analyzed to quantify the thickness of TGO and conformal reaction products (TGO + RP) layer and the local roughness of the TGO-alloy interface using a previously reported method.³⁹

RESULTS AND DISCUSSION

The general observations regarding the appearance of the specimens and the surface characterization are discussed first followed by a discussion of the reaction mechanisms for each deposit type. Finally, data from image analysis are used to discuss the prevalence of important degradation features and compare them to previously reported results for the deposit-induced degradation of FeCrAlY,^{38,39} which forms a single-layered α -Al₂O₃ TGO.

Baseline Behavior Without Deposits

Figure 1 shows the cross section of the TGO for the baseline specimen oxidized for 100 h without a deposit after the initial 100 h pre-oxidation. Absent a deposit, the Haynes-214 alloy formed a layered TGO with Ni(Cr,Al)₂O₄ spinel atop α -Al₂O₃ and a total thickness of \sim 4 μ m. The spinel layer was porous with increasing Al content moving inward towards the Al₂O₃. Occasional NiO nodules were observed in the Ni(Cr,Al)₂O₄ layer. The Al₂O₃ was

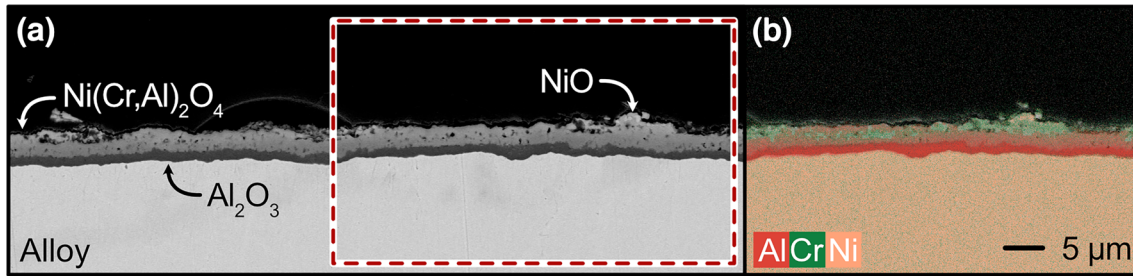


Fig. 1. Analysis of the oxidation products formed on the Haynes-214 baseline specimen. (a) BSE micrograph of a representative region and (b) corresponding EDS micrograph of the highlighted region.

thinner and denser than the spinel. A very limited number of oxide intrusions** into the alloy were observed and are attributed to alloy defects or surface contamination.

General Observations and Surface Characterization Following Deposit Exposure

Figure 2 shows the PSLS and Raman spectra for the specimens in regions away from the initial deposit locations. All the specimens exhibited the characteristic doublet of α - Al_2O_3 in the photoluminescence (PL) region. The shift in the α - Al_2O_3 doublet on the alloy relative to the α - Al_2O_3 powder standard is due to the residual growth stresses in the TGO.^{46,47} It is expected that the residual stress and the magnitude of the shift increase with TGO thickness. The α - Al_2O_3 doublet for the baseline sample shows the greatest leftward shift (highest stress) and the thickest TGO in the subsequent analysis. The reduced shift for the CMFAS-O sample could imply that there had been partial spallation in the representative location selected for the analysis. The Raman spectra confirm the presence of a $\text{Ni}(\text{Cr},\text{Al})_2\text{O}_4$ spinel;^{48–50} shifts in the peak positions for different specimens are due to the differences in Al content in the spinel or the residual growth stresses in the TGO.^{50,51}

All the deposits except the CNKMFAS – O $\bar{\text{S}}$ and CNKM – $\bar{\text{S}}$ shrank but remained solid and adhered to the specimen surfaces. The CNKMFAS – O $\bar{\text{S}}$ deposit formed a small fraction of melt due to the presence of low melting Na_2SO_4 . This melt spread to a region extending ~ 1 mm outside the initial deposit location. However, subsequent characterization showed no significant reaction of that melt with the TGO. The CNKM- $\bar{\text{S}}$ formed a large fraction of melt that spread across the complete specimen before the Na_2SO_4 evaporated. Photos of the specimens before and after the heat treatment are provided in Figure S1 in the supplementary material.

**We define an oxide intrusion to be oxide connected to the TGO that extends at least 1.5x deeper into the alloy than the average local TGO thickness.

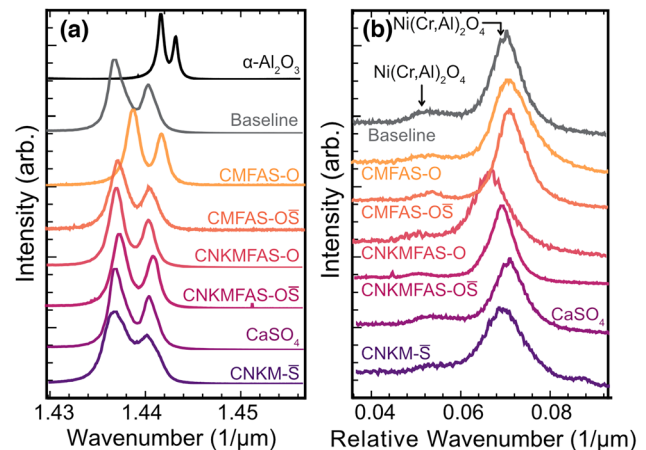


Fig. 2. (a) Photo-stimulated luminescence spectra (PSLS) and (b) Raman spectra in the $\text{Ni}(\text{Cr},\text{Al})_2\text{O}_4$ spinel region for the Haynes-214 specimens after heat treatment in the presence of deposits. The top line in (a) is from an α - Al_2O_3 powder standard.

Influence of Deposit Composition on Local Reactions

Reactions with Mixed Oxide Deposits

Figures 3 and 4 show representative cross sections of the specimen exposed to the CMFAS – O and CNKMFAS – O mixed oxide deposits, respectively. Away from the deposit, both specimens showed behavior like the baseline sample. The microstructures of the TGO under the two deposits were also like one another. The continuous alumina layer was intact and remained protective, but cracking or detachment of the outer spinel layer was more common than in regions away from the deposit. Where the outer spinel layer was still present, it tended to be more porous than the baseline (cf. Fig. 1 with Figs. 3b and 4b). Occasional particles of the residual deposit remain loosely attached, as shown in Fig. 3b. These comprise mixtures of the deposit components, e.g., Ca-rich silicates also containing some Mg, Fe, and Al, and some particles also contain Cr, typically with Mg, Al, and Fe. This suggests that the Cr from the spinel layer of the TGO reacted with components from the deposit. The implication is that the oxide deposits may locally adhere and increase the porosity in the

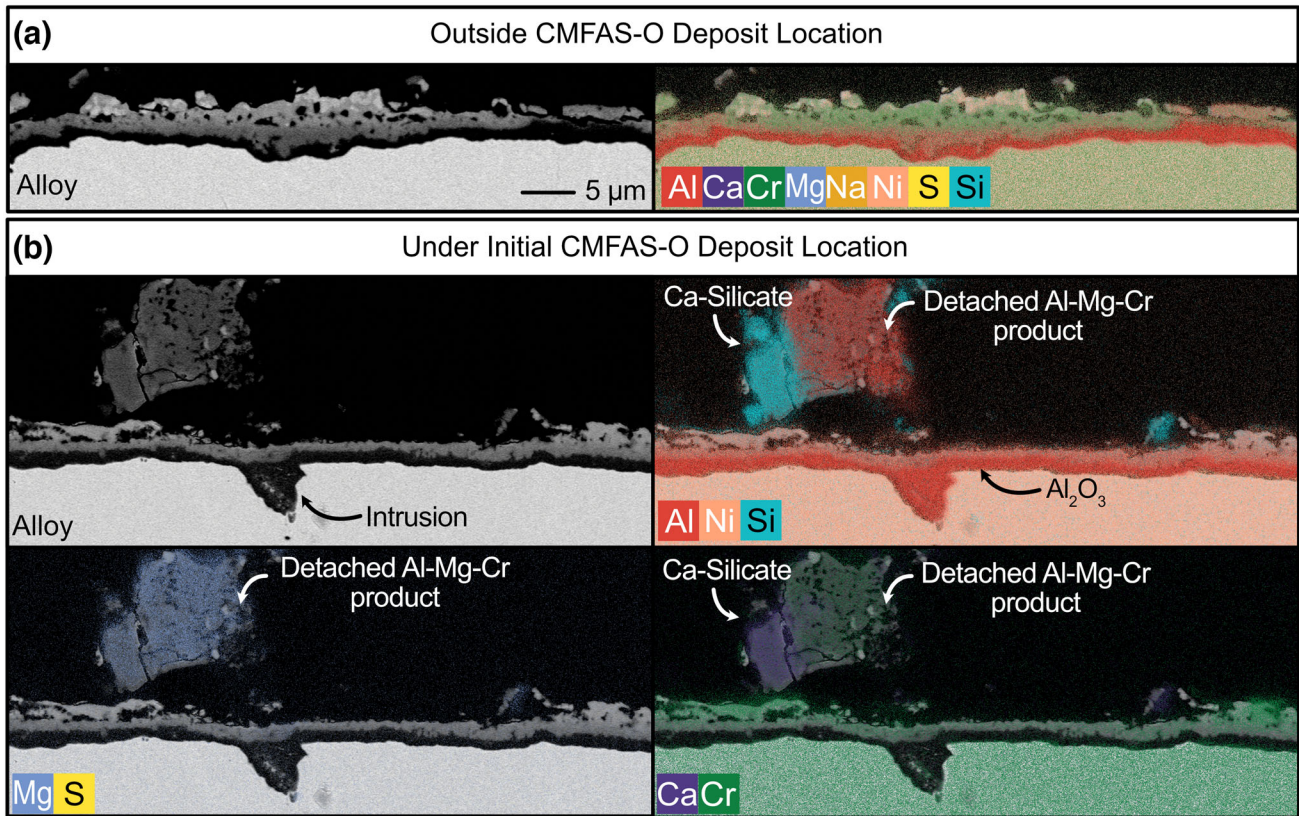


Fig. 3. BS-SEM micrographs and EDS analysis of the oxidation/corrosion products formed on the alloy exposed to CMFAS-O. (a) Region outside the initial deposit. (b) Region under the deposit. The upper left sub-panels show BSE images, and the remaining sub-panels show EDS maps of key elements overlaid on the BSE images.

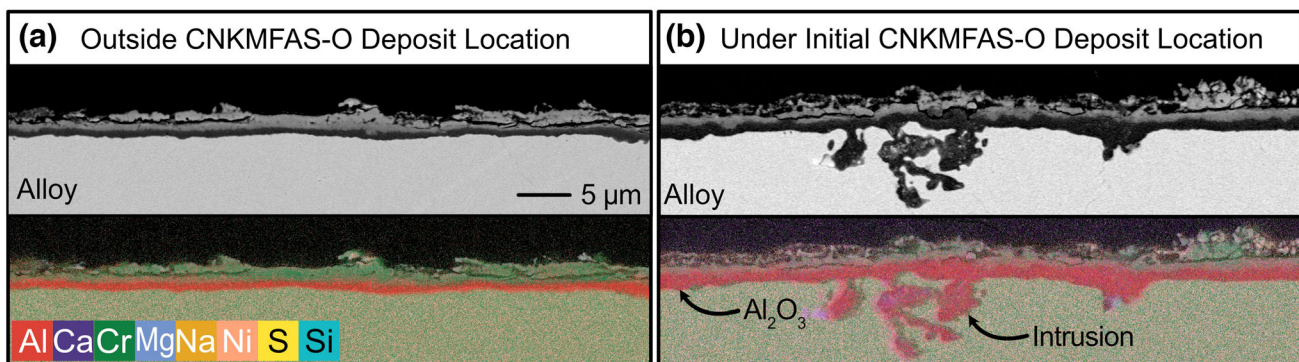


Fig. 4. Analysis of the oxidation/corrosion products formed on the alloy exposed to CNKMFAS-O. (a) Region outside the initial deposit. (b) Regions under the deposit. The top row in each panel shows BSE images, and the bottom row shows EDS maps of key elements.

spinel layer and its tendency to crack and delaminate, but the deposits do not appear to accelerate alloy oxidation. Furthermore, the addition of Na and K as oxides does not noticeably change the behavior.

Reactions with Oxide-Sulfate Deposits

Figures 5 and 6 show the typical behavior of the specimens exposed to the oxide-sulfate deposits. The general characteristics were similar to the mixed oxide deposits except, as elaborated below, there

was increased adherence of the Na-containing oxide-sulfate deposit compared to the other samples. The appearance of the TGO under the CMFAS – $O\bar{S}$ deposit (Fig. 5b) was similar to the CMFAS – O specimen suggesting that the presence of Ca and Mg as just oxides (CMFAS – O) or as a mixture of oxides and sulfates (CMFAS – $O\bar{S}$) does not significantly change the reactions with the TGO.

The addition of Na and K as a mixture of oxides and sulfates in the CNKMFAS – $O\bar{S}$ deposit increases the reactions with the TGO, leading to

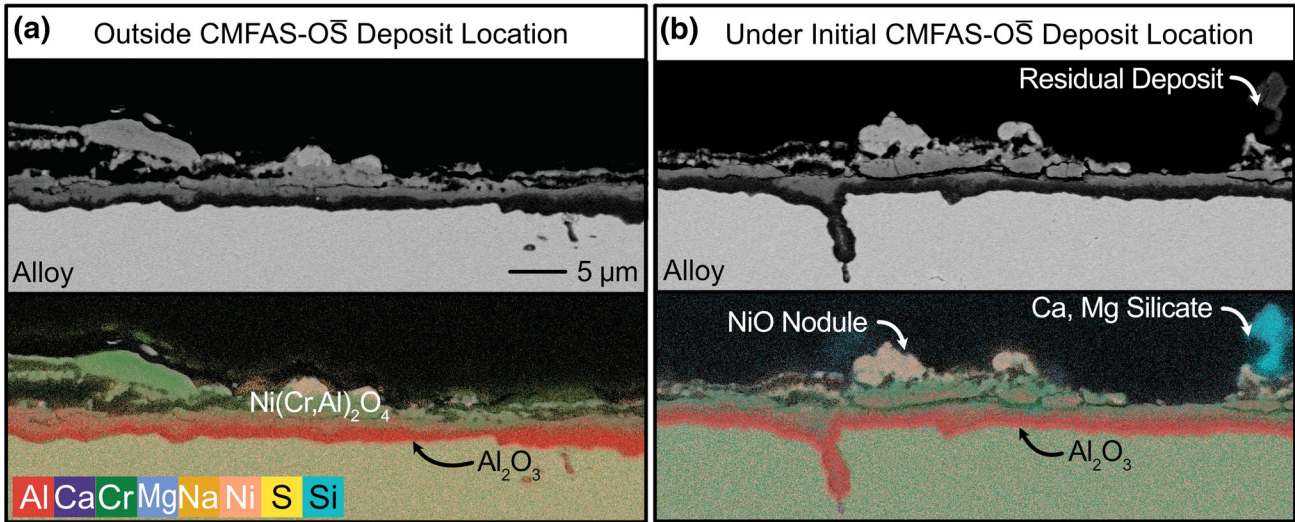


Fig. 5. Analysis of the oxidation/corrosion products formed on the alloy exposed to CMFAS-O₂. (a) Region outside the initial deposit. (b) Regions under the deposit. The top row shows BSE images, and the bottom row shows EDS maps of key elements.

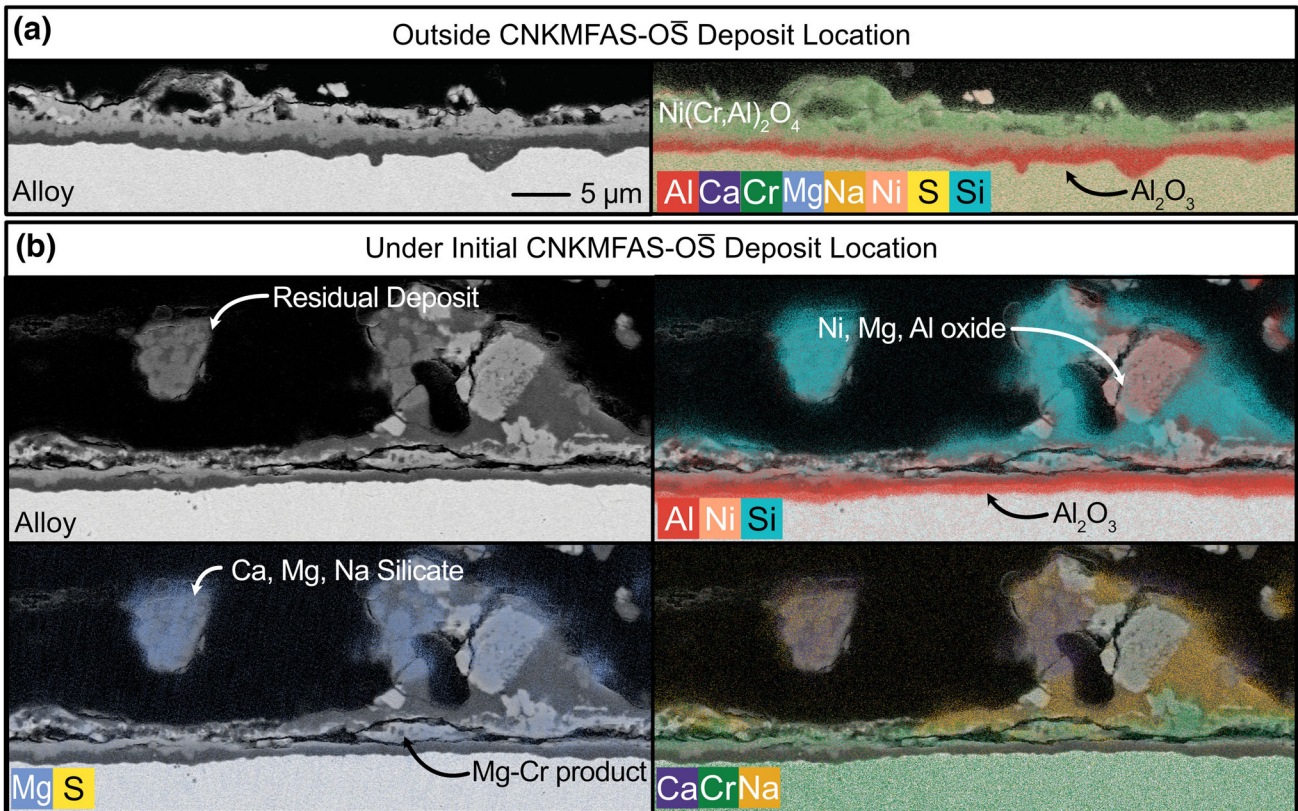


Fig. 6. Analysis of the oxidation/corrosion products formed on the alloy exposed to CNKMFAS-O₂. (a) Region outside the initial deposit. (b) Regions under the deposit. The upper left sub-panels show BSE images, and the remaining sub-panels show EDS maps of key elements overlaid on the BSE images

adherent reaction products and residual deposit (Fig. 6b). Some portions of the adhered material contained only components from the deposit (e.g., Ca- and Mg-rich silicates). Other portions contain elements from the spinel TGO (e.g., mixed Ni, Mg, Al oxides, and occasional Mg- and Cr-rich particles

intermixed with the spinel) surrounded by a continuous Na- and Ca-rich silicate. No sulfur was detected in these reaction products. The interpretation is that the Na₂SO₄, which melts during the initial heating, drives reactions that partially dissolve the spinel TGO layer. Subsequent reactions

with the oxide components in the deposit convert the Na_2SO_4 into a mixture of Na-containing silicates. Despite these reactions, the underlying $\alpha\text{-Al}_2\text{O}_3$ TGO remains intact, and there is no evidence of accelerated alloy degradation compared to the oxide deposits.

The overall similarity between oxide and oxide-sulfate deposits reemphasizes that the presence of the oxides in mixed oxide-sulfate deposits accelerates the sulfate decomposition into oxides,^{38,40} thereby limiting the propensity for the more severe sulfate-induced degradation described in the subsequent sections. The one notable difference is between CNKMFAS – O and CNKMFAS – OS, where the latter shows evidence of melt-mediated reactions. Previously reported thermodynamic calculations showed that both deposits have an equilibrium solidus temperature of 1065°C ,⁴⁰ which is above the melting temperature of 884°C for Na_2SO_4 ¹⁶ and 650°C for the $\text{MgSO}_4\text{-Na}_2\text{SO}_4\text{-CaSO}_4$ eutectic.⁵² The difference is ascribed to the fact that in the equilibrium calculations, the sulfates are predicted to decompose via reactions with the oxides before reaching the sulfate melting temperature. However, related calculations in which the sulfate decomposition is temporarily suppressed by limiting the rate of removal of gaseous SO_2 and SO_3 showed that a transient melt could form at or below 1025°C .⁴⁰ The observed formation of melt in the current experiments suggests that these reactions

are not fast enough to prevent transient melt formation upon heating the mixed deposits.

Reactions with CaSO_4 Deposit

Figure 7 shows representative cross-section BSE micrographs and EDS maps of the specimens exposed to CaSO_4 . Regions away from the deposit retained the dual-layered $\alpha\text{-Al}_2\text{O}_3$ and spinel TGO with no evidence of reaction with the CaSO_4 (Fig. 7c). Under the deposit, the TGO reacted with CaSO_4 to form a mixture of reaction products divided into several layers. The outer layer consisted of CaO , CaSO_4 , and $\text{Ca}_x\text{Cr}_y\text{O}_z$, similar to those reported in Refs. 32 and 33. Moving inward, calcium chromate becomes the primary phase with occasional inclusions of NiO and Ca-rich aluminates (likely $\text{Ca}_3\text{Al}_2\text{O}_6$ and $\text{C}_{12}\text{Al}_{14}\text{O}_{33}$ based on semi-quantitative EDS and comparison to the binary phase diagram^{29,30,32}). The next layer consists primarily of calcium aluminates, transitioning from $\text{C}_{12}\text{Al}_{14}\text{O}_{33}$ to the Ca-lean CaAl_2O_4 adjacent to a thin Al_2O_3 layer. These observations align with previous reports of the CaSO_4 -induced corrosion of other Ni-containing, Al_2O_3 -forming alloys.^{31,53} The Al_2O_3 is relatively continuous and appears protective along most of the alloy/TGO interface, although internal oxidation was evident in some places (Fig. 7a and b-I).

At a few locations the CaSO_4 caused a more aggressive attack producing thicker nodules of mixed $\text{Ca}_x\text{Cr}_y\text{O}_z$, $\text{Ca}_x\text{Al}_y\text{O}_z$, and NiO (Fig. 7a and

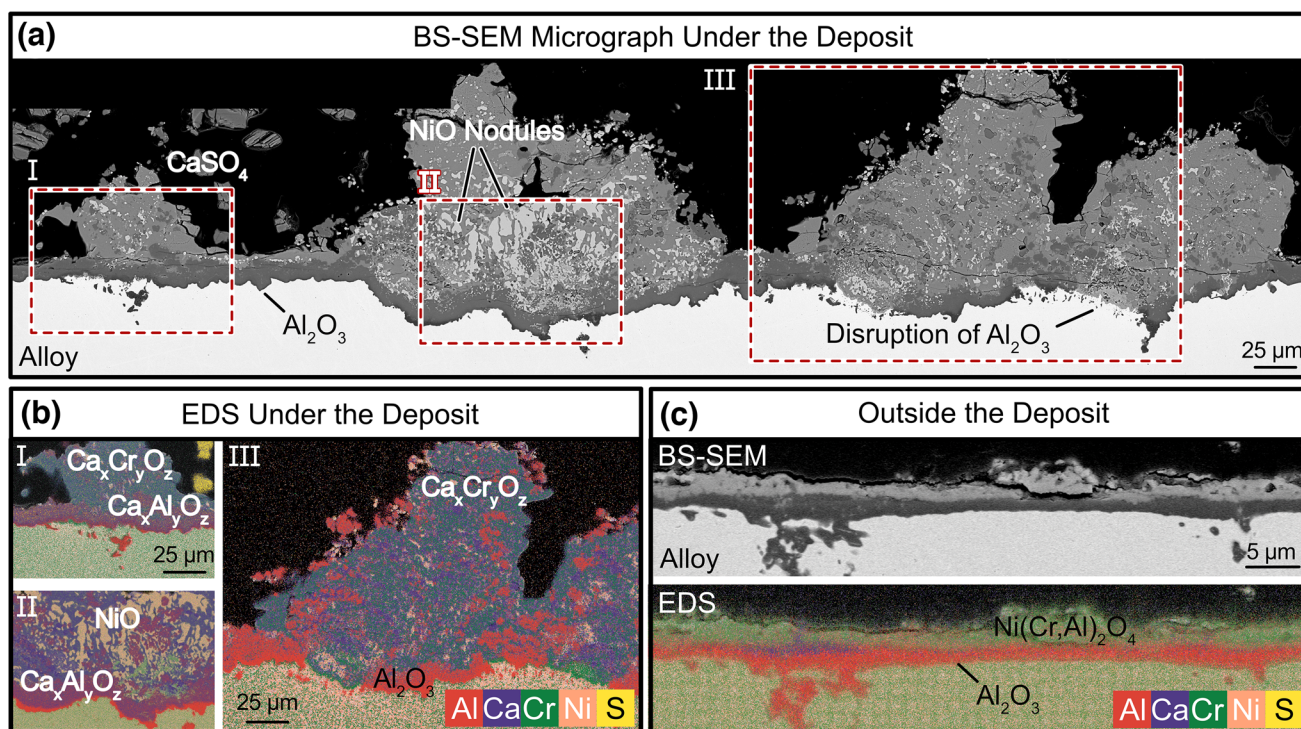


Fig. 7. Analysis of the oxidation/corrosion products formed on the alloy exposed to the CaSO_4 deposit in (a, b) region under the deposit with (a) showing the BS-SEM merged micrographs and (b) showing the EDS maps of key elements in the highlighted regions and (c) region outside the deposit. Parts (a) and (b) are at the same magnification.

b-II and III)). A continuous layer of $\text{Ca}_x\text{Al}_y\text{O}_z$ products forms between the thick, mixed nodules and a discontinuous layer of Al_2O_3 at the alloy/TGO interface. Where the Al_2O_3 was disrupted, a Cr_2O_3 layer formed at the alloy/RP interface. Internal Al oxidation was often evident in such locations. No internal sulfidation was observed, even at locations with more aggressive attacks.

The predominant behavior (Fig. 7b) is explained by reactions between the spinel layer and CaSO_4 that convert the spinel to less-protective $\text{Ca}_x\text{Cr}_y\text{O}_z$. The $\text{Ca}_x\text{Al}_y\text{O}_z$ inclusions in the $\text{Ca}_x\text{Cr}_y\text{O}_z$ layer are likely formed from the Al dissolved in the spinel; the NiO from the spinel does not react with the CaSO_4 and instead forms NiO inclusions. As Ca diffuses inward it reacts with the Al_2O_3 to form the continuous $\text{Ca}_x\text{Al}_y\text{O}_z$ layer. The mechanism leading to the variations in the degree of reaction may be attributed to a combination of local variations in the initial spinel thickness or transient melt formation that disrupts the initial Al_2O_3 TGO layer. For instance, the presence of excess Cr in a thicker spinel layer could push the system into the 1022°C

eutectic reaction between $\text{Ca}_9\text{Cr}_6\text{O}_{24}$ and $\beta\text{-CaCr}_2\text{O}_4$.³²

Reactions with CNKM- $\bar{\text{S}}$ Deposit

Figure 8 shows the cross-section BSE and EDS maps of the specimens exposed to CNKM- $\bar{\text{S}}$. Since the deposit melted and spread, there was significant reaction with the TGO in regions away from the initial deposit location. Based on the comparison of the EDS data with reported stable phases,^{32,33,54-57} the predominant reaction products consisted of mixed $\text{Ca}_x\text{Cr}_y\text{O}_z$, $\text{Mg}_x\text{Cr}_y\text{O}_z$ (either MgCr_2O_4 or Mg-saturated Cr_2O_3), and $\text{Ca}_x\text{Al}_y\text{O}_z$. In regions outside the initial deposit location (see Fig. 8a), the reaction products consisted of a mixture of $\text{Ca}_x\text{Cr}_y\text{O}_z$, $\text{Mg}_x\text{Cr}_y\text{O}_z$, and $\text{Ca}_x\text{Al}_y\text{O}_z$. At some locations, the RP layer mainly consisted of $\text{Mg}_x\text{Cr}_y\text{O}_z$ and $\text{Ca}_x\text{Al}_y\text{O}_z$, with detached $\text{Ca}_x\text{Cr}_y\text{O}_z$ products suggesting that the spinel was dissolved by the transient melt and reprecipitated as RPs. Ni did not participate in the reactions and segregated out as NiO nodules, similar to the specimen exposed to the CaSO_4 deposit.

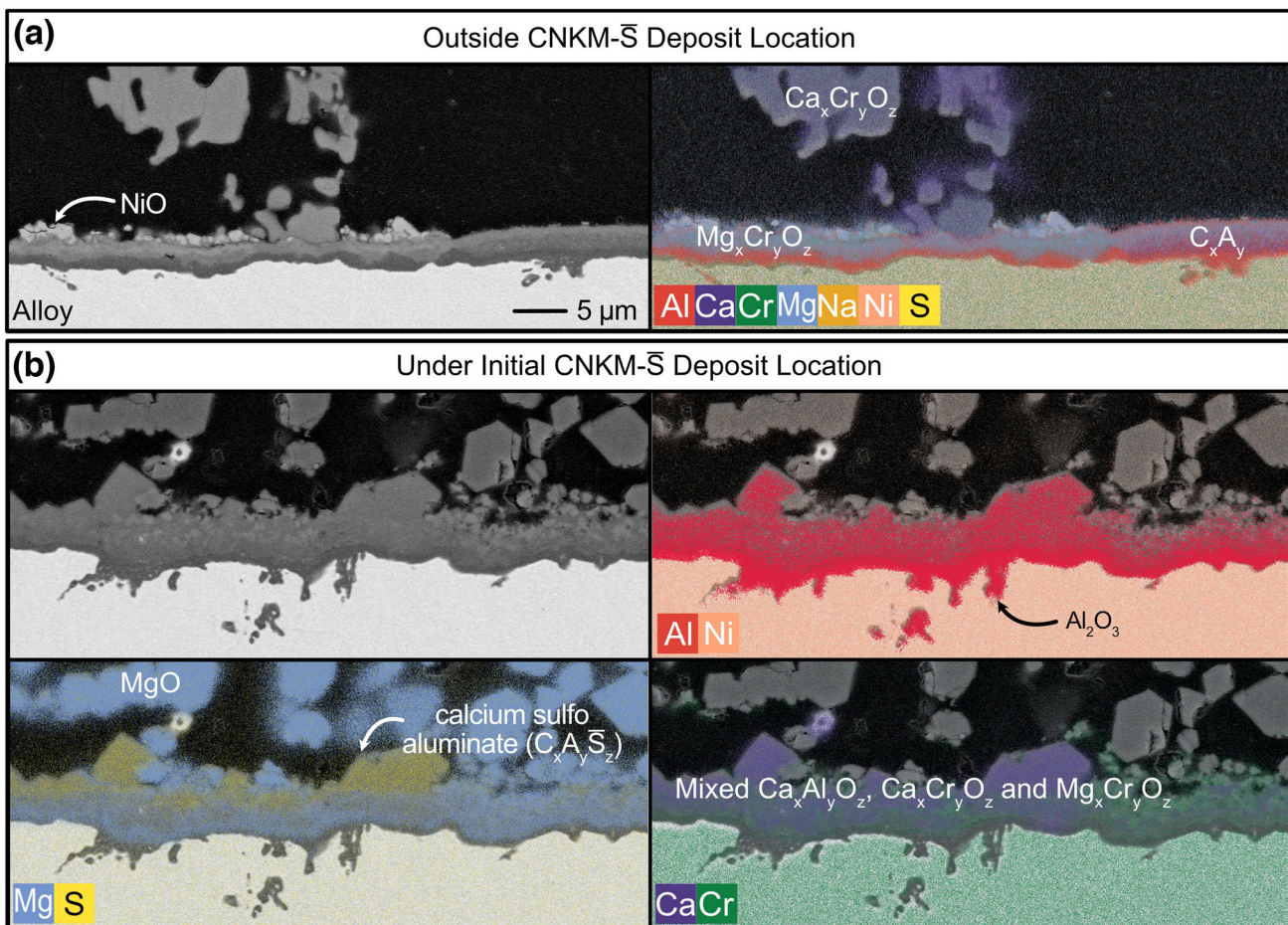


Fig. 8. Analysis of the oxidation/corrosion products formed on the alloy in region under the CNKM- $\bar{\text{S}}$ deposit. (a) Region outside the initial CNKM- $\bar{\text{S}}$ deposit. (b) Regions under the CNKM- $\bar{\text{S}}$ deposit. The upper left sub-panels show BSE images, and the remaining sub-panels show EDS maps of key elements overlaid on the BSE images.

In regions under the deposit, the outer portion of the reaction layer consisted of calcium sulfoaluminate (approximately $\text{Ca}_4\text{Al}_6\text{O}_{12}\text{SO}_4$), followed by a thick layer of $\text{Ca}_x\text{Cr}_y\text{O}_z$, $\text{Mg}_x\text{Cr}_y\text{O}_z$, and mixtures of $\text{Ca}_x\text{Al}_y\text{O}_z$. Below these reaction products, the Al_2O_3 at the alloy interface continued to protect the alloy. The $\text{Mg}_x\text{Cr}_y\text{O}_z$ layer was often observed adjacent to the Al_2O_3 layer. The reaction layer architecture suggests that the Mg in the deposit reacts preferentially with Cr to form the dense, relatively continuous $\text{Mg}_x\text{Cr}_y\text{O}_z$ layer while reducing the tendency to form the less protective $\text{Ca}_x\text{Cr}_y\text{O}_z$. Additionally, the presence of $\text{Mg}_x\text{Cr}_y\text{O}_z$ adjacent to the Al_2O_3 layer reduces the reaction between Ca and Al to form the $\text{Ca}_x\text{Al}_y\text{O}_z$, thereby limiting the RP layer thickness and alloy recession.

In the deposit layer adjacent to the RP, MgO nodules were observed suggesting that MgSO_4 decomposed during the melting and spreading and precipitated out as MgO predominantly in the region under the initial deposit (see Fig. 8b). Na and K were not observed in the reaction products or in the residual deposit. This suggests that even though the Na and K salts facilitated the melting and spreading of the deposit (and the subsequent partial dissolution of the spinel), they ultimately volatilize rather than forming reaction products with components from the TGO. A key distinction compared to the experiments with the oxide-sulfate deposits is that the sodium does not persist in this case; it only stabilized in the residual deposit and reaction product layer in the presence of silicates.

Quantitative Analysis of Degradation Features

Effect on the TGO + RP Thickness

Figure 9 shows the TGO and TGO + RP thicknesses as a function of position across the cross section for each specimen. Except for occasional spikes in the TGO + RP thickness, which represent the oxide intrusions in the alloy, the TGO thickness was relatively uniform for the baseline specimen (Fig. 9a) and for specimens exposed to the oxide (Fig. 9b, c) and oxide-sulfate (Fig. 9d, e) deposits. Comparing the thickness outside and under the initial oxide and oxide-sulfate deposit location, we observe the TGO + RP thickness under each deposit is slightly lower than outside of the deposit. This is attributed to the increased cracking and delamination of the spinel layer under the deposits. No significant increase in the oxide intrusions was observed under these deposits.

In comparison, the formation of calcium chromates and aluminates upon reaction with CaSO_4 roughly triples the TGO + RP thickness across the area under the initial deposit location (Fig. 9f). The local increase in the TGO + RP thickness represents the oxide intrusions in the alloy, whereas the broad regions with TGO + RP thickness substantially

higher than the average behavior correspond to a location with aggressive attack shown in Fig. 7a and bII and III. Since the solid deposit did not spread, the TGO + RP thickness away from the initial deposit location is close to the baseline behavior. Figure 9f shows the increased TGO + RP across the entire specimen caused by the molten $\text{CNKM} - \bar{\text{S}}$ deposit. In contrast to the CaSO_4 deposit, the attack in the presence of $\text{CNKM} - \bar{\text{S}}$ was more uniform with a lower frequency of the deep oxide intrusions into the alloy and comparatively lower TGO + RP thickness. This behavior is likely due to the formation of $\text{Mg}_x\text{Cr}_y\text{O}_z$, which shields underlying Al_2O_3 TGO from forming thicker $\text{Ca}_x\text{Al}_y\text{O}_z$ and $\text{Ca}_x\text{Cr}_y\text{O}_z$ and prevents the associated alloy recession. The attack of the $\text{CNKM} - \bar{\text{S}}$ deposit diminishes towards the specimen edges, possibly due to the depletion of reactants as the melt spreads.

Table II summarizes the average (\pm standard deviation) and median TGO + RP thickness for each specimen region. The median TGO + RP thickness in the presence of the deposits is generally lower than the average owing to the presence of many locations with TGO + RP thickness greater than the mean, with few regions of TGO spallation. The uniform reaction of the molten $\text{CNKM} - \bar{\text{S}}$ deposit across the alloy increased both the average and median TGO + RP thickness in both the sample regions as compared to the baseline. Vigorous reaction of the CaSO_4 deposit at specific locations led to higher average TGO + RP thickness under the deposit as compared to the median value.

The position specific TGO + RP thickness data are plotted as cumulative probability distributions (CPD) in Fig. 10. The shaded baseline region (see Fig. 10a) was defined by performing an experiment without deposits and the knowledge of typical variation in the TGO thickness as a function of minor changes in the sample positioning in the furnace.³⁸ Except for the specimen exposed to $\text{CNKM} - \bar{\text{S}}$ deposit, the region outside the initial deposit location exhibited narrow thickness distributions falling within the baseline region. The spreading of the molten $\text{CNKM} - \bar{\text{S}}$ drove the reaction in regions outside the initial deposit location leading to an increase in the TGO + RP thickness, thus shifting the CPD curve to the right. The CPDs under the mixed oxide and oxide-sulfate deposits fall in the baseline region but have slightly shifted towards lower thickness compared to the regions outside the deposit because of the increased delamination of the spinel layer (see Fig. 10b). The CPD for the region under the $\text{CNKM} - \bar{\text{S}}$ is similar to that away from the initial deposit since it spread and reacted uniformly. The shape of the CPD for the region under the CaSO_4 deposit changes relative to the other specimens since the reactions to form $\text{Ca}_x\text{Cr}_y\text{O}_z$ and $\text{Ca}_x\text{Al}_y\text{O}_z$ significantly increase the TGO + RP thicknesses.

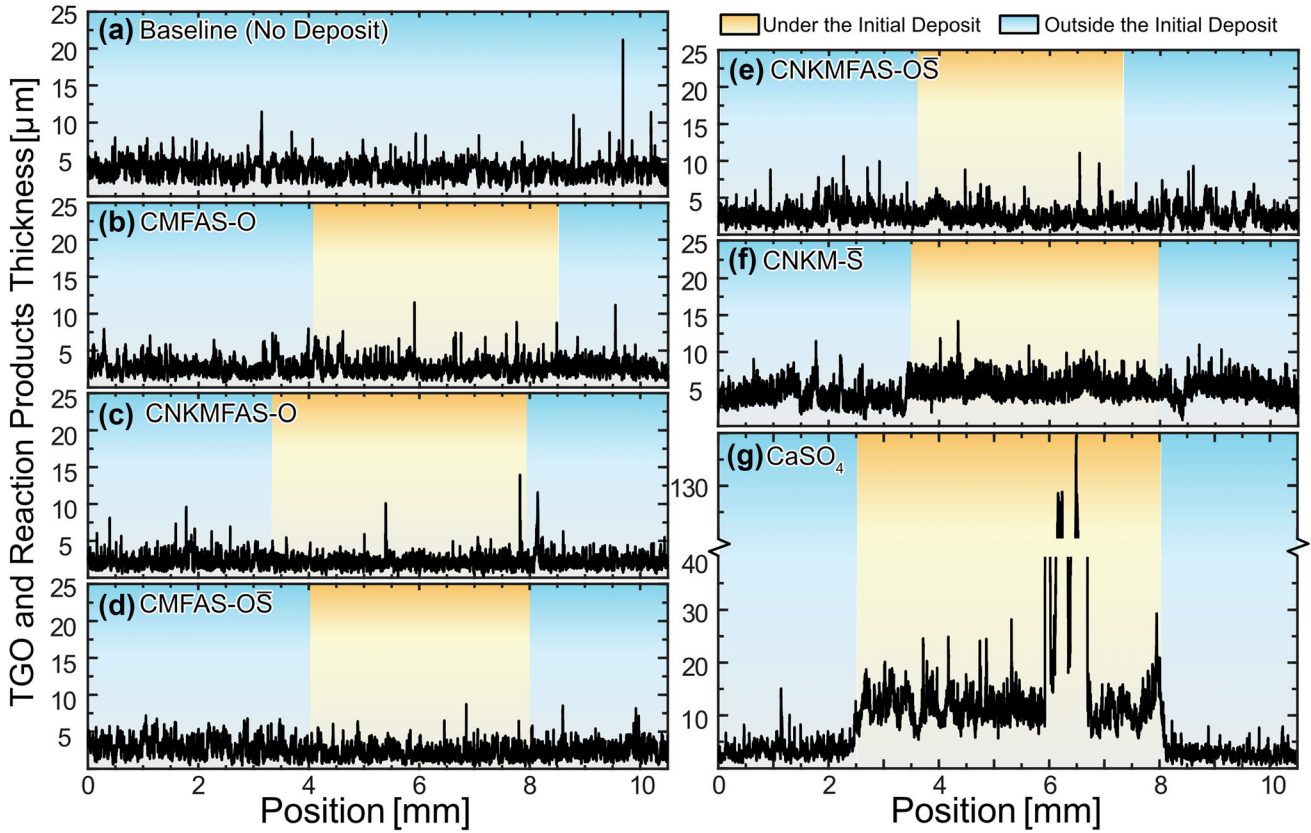


Fig. 9. Plots of the TGO + RP thickness as a function of position across the Haynes-214 specimen for the (a) baseline and after exposure to (b) CMFAS-O, (c) CNKMFAS-O, (d) CMFAS-O \bar{S} , (e) CNKMFAS-O \bar{S} , (f) CNKM- \bar{S} , and (g) CaSO_4 deposits at 1025°C for 100 h. The ordinate scale in all panels is equivalent except for (f), which is expanded to show the thicker reaction product regions.

Table II. Average (\pm standard deviation) and median TGO + RP thickness (in μm) on the Haynes-214 alloy after exposure to different deposits

Deposit	Outside initial deposit		Under initial deposit	
	Average	Median	Average	Median
None (baseline)	3.3 ± 1.1	3.3	—	—
CMFAS-O	2.7 ± 0.98	2.5	2.7 ± 1.0	2.5
CNKMFAS-O	2.8 ± 1.2	2.1	2.1 ± 0.8	2.0
CMFAS-O \bar{S}	2.6 ± 1.1	2.5	2.1 ± 0.9	2.0
CNKMFAS-O \bar{S}	2.6 ± 1.1	2.3	2.4 ± 0.98	2.3
CaSO_4	3.0 ± 1.3	2.8	20.3 ± 26.3	11.8
CNKM- \bar{S}	4.4 ± 1.3	4.2	5.4 ± 1.3	5.3

To understand the effect of the reactions involving Cr on the total TGO + RP thickness, Fig. 10c, d compares the CPD for the Haynes-214 and FeCrAlY alloy^{38,39} exposed to CaSO_4 and CNKM- \bar{S} . The baseline CPDs for FeCrAlY and Haynes-214 are similar, although the FeCrAlY curve is steeper and generally to the left of that for Haynes-214 because of the added thickness and variability in the spinel layer in the latter. The CPDs for both the specimens away from the CaSO_4 deposit fall close to the respective baseline curves. Under the CaSO_4

deposit, both shift towards a higher TGO + RP thickness but the shift for the Haynes-214 alloy is more than a factor of two greater than FeCrAlY. The last 20% of the distribution on Haynes-214 is extremely broad, extending up to 130 μm , because of the regions with aggressive degradation. These observations highlight the important role of Cr in the TGO in accelerating hot corrosion by CaSO_4 . In contrast, for the specimens exposed to CNKM- \bar{S} , the CPD curves for the regions under the deposit are nearly coincident for the two alloys. Outside the

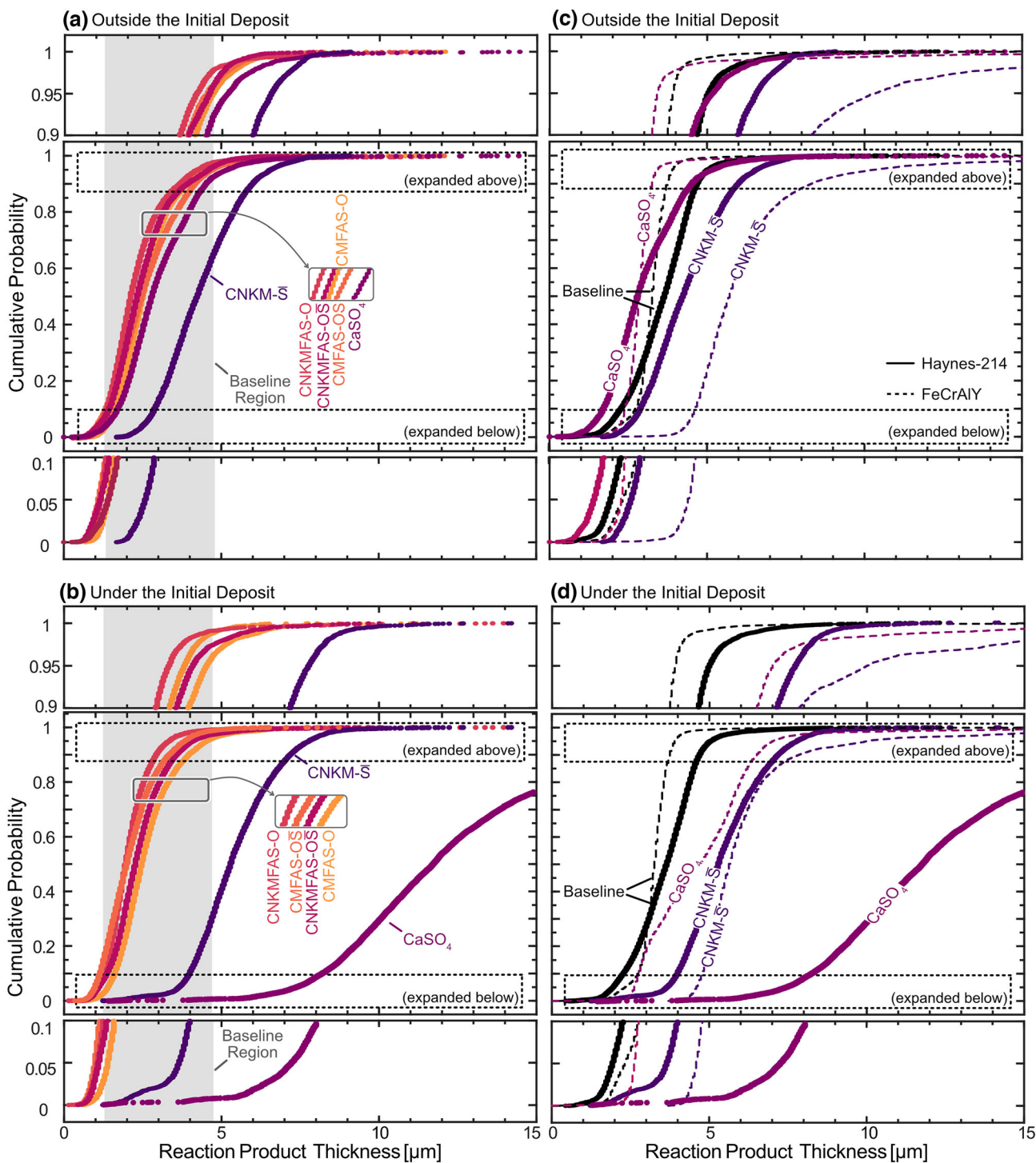


Fig. 10. Cumulative probability distributions of the TGO + RP thickness (a, c) outside and (b, d) under the initial deposit position for the (a, b) Haynes-214 specimens exposed to all deposits and (c, d) selected comparison to FeCrAlY data from Ref. 38.

initial deposit location, the CPD for FeCrAlY is shifted towards higher thickness than for Haynes-214. This observation supports the hypothesis that the formation of $Mg_xCr_yO_z$ due to the presence of Mg in the CNKM – S deposit prevents the interaction of Al_2O_3 with $CaSO_4$ and reduces the severity of the corrosion on Haynes-214.

Effect on the Interface Roughness

Figure 11 shows variations in the alloy-TGO interface position as a function of location across the cross section of each specimen. Higher amplitude variations correspond to increased interface roughening. The calculated average (R_a) and root mean squared (R_q) roughness are shown in Fig. 12;

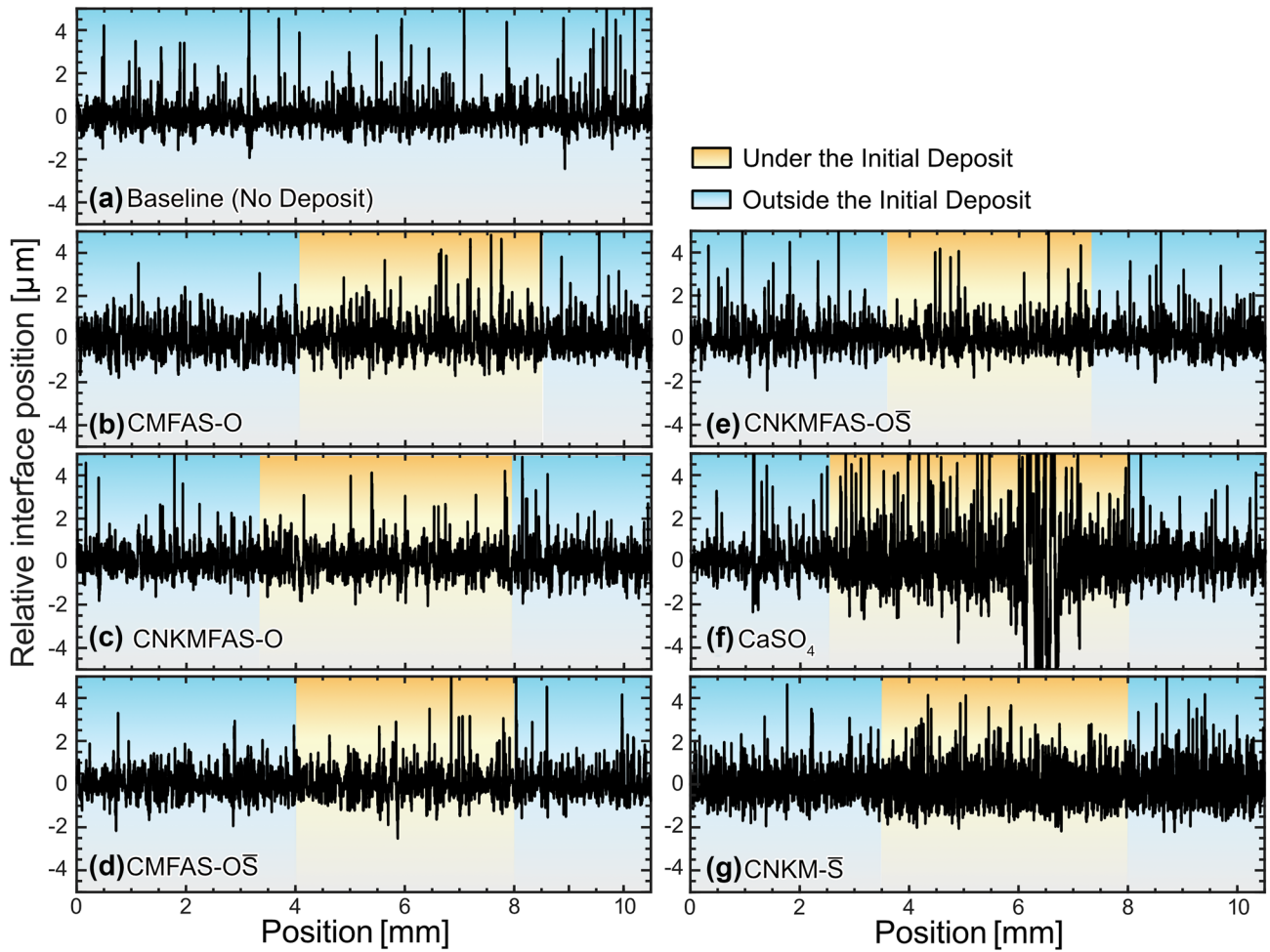


Fig. 11. Plots of relative interface position as a function of location across the Haynes-214 specimen for the (a) baseline and after exposure to (b) CMFAS-O, (c) CNKMFAS-O, (d) CMFAS-O S̄, (e) CNKMFAS-O S̄, (f) CaSO₄, and (g) CNKM-S̄ deposits at 1025°C for 100 h.

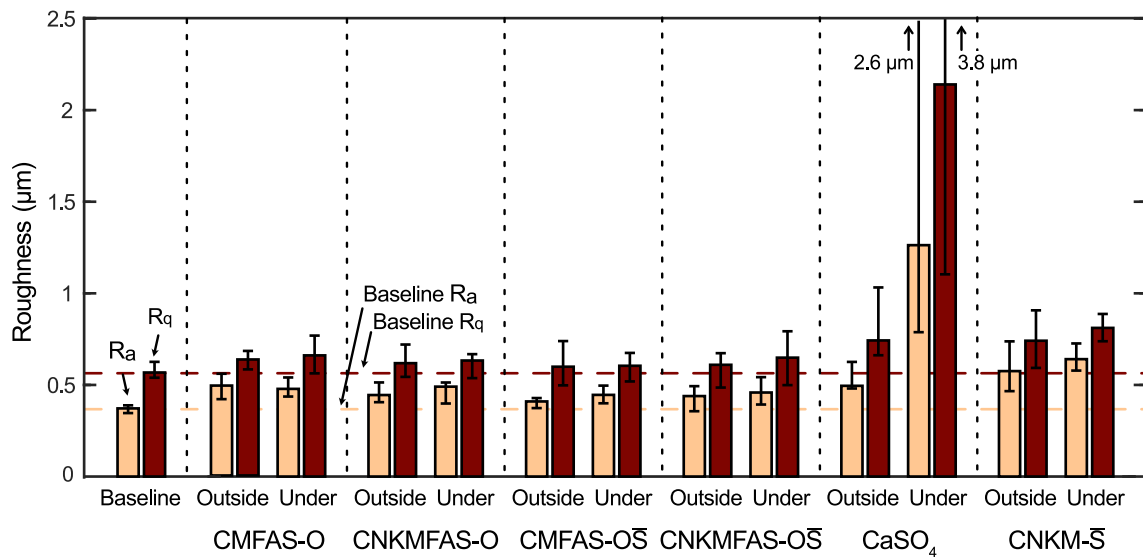


Fig. 12. Variation in the average roughness (R_a) and the root mean squared (RMS, R_q) roughness under the deposit and outside the deposit.

the error bars correspond to the maximum and minimum R_a and R_q values respectively in a set of 20 random subsets each containing 25% of the cross section length in respective regions. For all the specimens except the one exposed to CNKM – \bar{S} , the relative interface height in the region outside the initial deposit location was uniform and comparable to the baseline behavior. For the specimen exposed to mixed oxide and oxide-sulfate deposits, the relative interface height under the deposit did not change as compared to the area outside the initial deposit location (Fig. 11 b–e). Similarly for the specimens exposed to the mixed oxide and oxide-sulfate deposits the R_a and R_q values are comparable to the baseline. Under the CaSO_4 deposit, the interface roughness increased compared to the region outside owing to the formation of less protective calcium chromates and aluminates. Sharp increases in the interface roughness $> 4 \mu\text{m}$ correspond to the regions of aggressive attack with significant alloy recession. The sharp increase in the interface heights in regions of aggressive attack also increases the R_a and R_q values and their variation as shown by the error limits. The interface roughness was uniform across the specimen exposed to the CNKM – \bar{S} but greater than the baseline behavior.

CPDs for the interface roughness data are plotted in Fig. 13a, b for regions outside and under the initial deposit respectively. A curve with a shallower slope and wider distribution is associated with increased interface roughness. In areas outside the deposit, all specimens except CNKM – \bar{S} closely follow the baseline distribution ranging from $-1.5 \mu\text{m}$ to $2 \mu\text{m}$. The CNKM – \bar{S} specimen shows increased roughness (by 59% compared to average baseline roughness) because of the reactions with the molten deposit outside the initial deposit location.

The CPDs for regions under the mixed oxide and oxide-sulfate deposits (see Fig. 13b) also mimic the baseline behavior. In comparison, the formation of thick, less-protective reaction products in the presence of the CaSO_4 and CNKM – \bar{S} deposits produced rougher interfaces (240% and 78% increase, respectively, compared to average baseline roughness), broadening the CPD. The specimen exposed to CaSO_4 was skewed towards higher roughness due to either variation in the spatial oxidation rate or generation of growth stresses as a result of the formation of thicker reaction products.

Figure 13c, d compares the CPD for Haynes-214 and FeCrAlY alloys exposed to CaSO_4 and CNKM – \bar{S} and their respective baselines. Haynes-214 has a higher interface roughness than FeCrAlY alloy in the baseline specimens. This difference is magnified by the reactions with the deposits, with the Haynes-214 specimens showing a more significant increase

in interface roughness under the CNKM – \bar{S} and CaSO_4 deposits compared to FeCrAlY. The implication is that the extensive reactions with the TGO on Haynes-214 to form thick chromates and aluminates also increase the roughness of the alloy interface under the intact Al_2O_3 TGO layer.

Implications for the Deposit-Induced Degradation of Alloys

The results provide quantitative information about the effect of TGO structure and composition on the hot corrosion and TGO reactions. The oxide and oxide-sulfate deposits do not react with the TGO on the Haynes-214 alloy except for localized reactions with the spinel layer that promote its delamination. The effect was particularly evident for the CNKMFAS – $\text{O}\bar{S}$ deposit where the transient presence of low melting sulfates facilitated local reactions with the spinel. The implication is that the presence of oxides in the deposit reduces the corrosive effects of the sulfates in mixed oxide-sulfate deposits. Therefore, the most severe component degradation is likely to occur in service conditions where the ingested debris comprises primarily sulfates such as in regions with high concentrations of sulfate minerals (e.g., gypsum sands) or sulfur-rich industrial pollutants.

The results also show that for the deposits that are rich in CaSO_4 , the presence of Cr in the TGO increased the attack intensity as compared to the FeCrAlY alloy. A major contributing factor is likely the formation of calcium chromates on reaction with the spinel TGO on the Haynes-214 alloy. Some locations under the deposit on Haynes-214 showed disruption of underlying Al_2O_3 TGO possibly due to excessive TGO consumption in spinel-rich regions. The implication is that the presence of Cr-rich TGO is undesirable in the presence of a Ca-rich deposit; therefore, alloy designs that achieve good Al_2O_3 formation with lower Cr content are desirable.

An additional objective of the study was to understand how the presence of lower melting sulfates in a CaSO_4 -based deposit changes the hot corrosion behavior compared to a solid CaSO_4 deposit. The results show that even though the CNKM – \bar{S} melted and spread, and therefore affected more of the overall sample surface, it formed thinner mixed calcium aluminates, chromates, and magnesium chromate products compared to the thick, less-protective calcium chromate and aluminate reaction products formed by CaSO_4 alone. The reaction layer architecture implies that Mg in the deposit competes with Ca to form chromates and that the magnesium chromate layer limited the interaction of Ca with the underlying Al_2O_3 layer. Ni did not take part in the reactions and segregated in the TGO + RP layer as NiO nodules or inclusions.

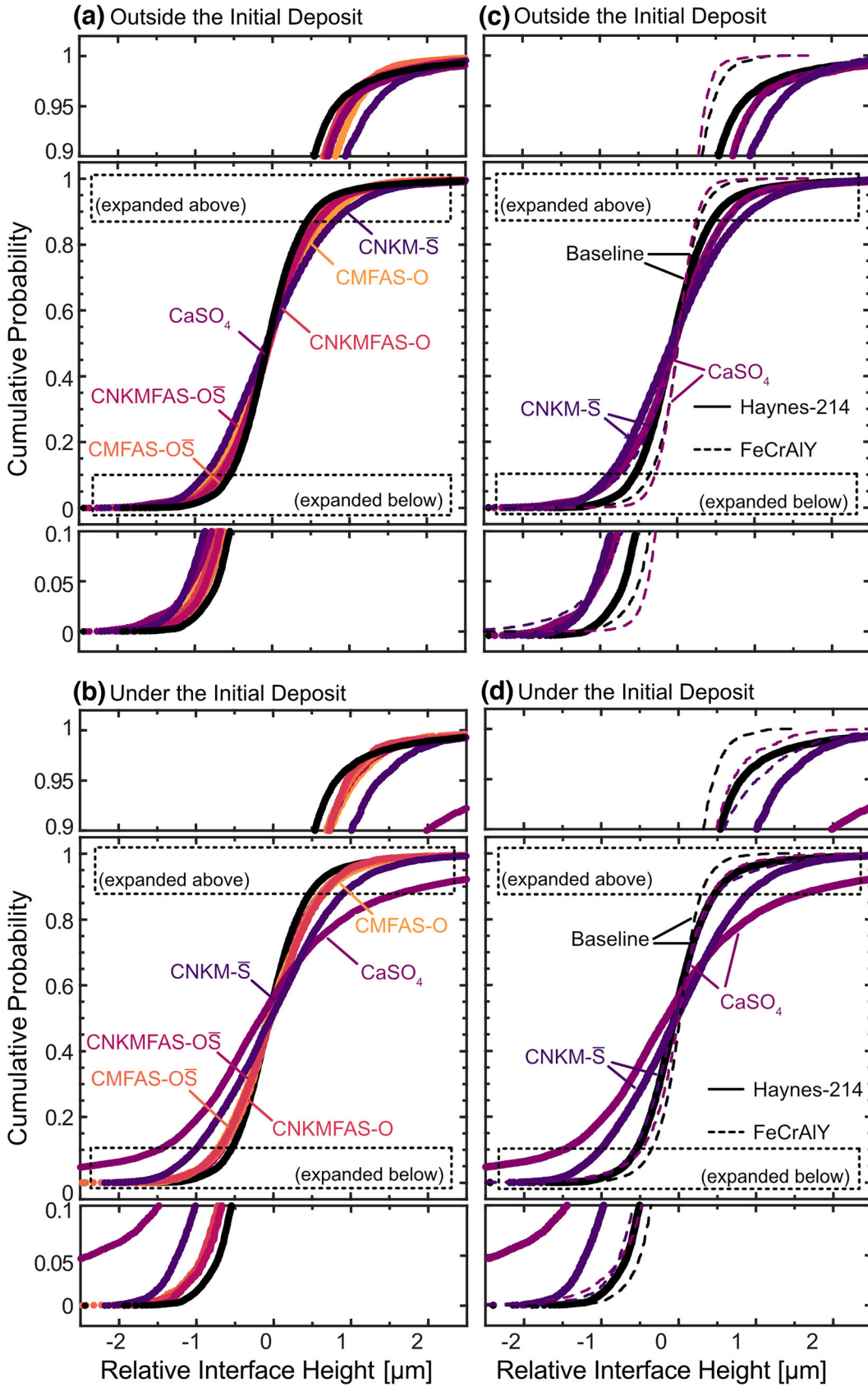


Fig. 13. CPD of the interface roughness (a, c) outside and (b, d) under the initial deposit position for the Haynes-214 and FeCrAlY specimens. FeCrAlY data from Ref. 38.

CONCLUSION

This work utilized a combination of local microstructure characterization and image analysis to improve the understanding of the effect of minor elements in the TGO on the accelerated corrosion in the presence of oxide, oxide-sulfate, and sulfate deposits. Key conclusions are:

1. The oxide and oxide-sulfate deposits did not react significantly with the TGO on the Haynes-214 alloy but increased the delamination of the spinel layer under the deposit. The oxide and oxide-sulfate deposits with Na and K were more likely to adhere to the TGO and cause the spinel layer to crack. Although neither the sulfate-free oxide deposits nor the mixed oxide-sulfate deposits caused severe attack, there was more evidence of deposit reaction in the latter due to the transient Na_2SO_4 melt.
2. The CaSO_4 and $\text{CNKM} - \bar{\text{S}}$ deposits reacted more significantly with the TGO than the oxide-containing deposits. The solid CaSO_4 only formed RP layers under the initial deposit location while the molten $\text{CNKM} - \bar{\text{S}}$ deposit spread and reacted with TGO across the entire surface of the sample.
3. The formation of calcium chromate in the presence of CaSO_4 led to much thicker reaction product layers than Al_2O_3 forming FeCrAlY alloy exposed to the same deposit significant reaction. In some locations, the reaction was sufficiently severe to disrupt the inner Al_2O_3 layer on Haynes-214 leading to internal oxidation.
4. The presence of Mg in $\text{CNKM} - \bar{\text{S}}$ deposit led to the formation of magnesium chromate just above the underlying Al_2O_3 TGO and limited the formation of calcium chromate. Moreover, lack of interaction between Mg and Al prevented Al consumption because of the formation of calcium aluminates and led to a thinner TGO + RP layer that did not disrupt the underlying Al_2O_3 TGO layer.

SUPPLEMENTARY INFORMATION

The online version contains supplementary material available at <https://doi.org/10.1007/s11837-024-06599-y>.

ACKNOWLEDGEMENTS

The authors are grateful to Dr. Eeshani Godbole for assistance in preparing the deposit powders. The alloy material was kindly provided by Haynes International, Inc.

FUNDING

This research was supported by the Office of Naval Research (award number N68335-20-C-0472 monitored by Dr. David Shifler) via a subaward from QuesTek Innovations LLC. Part of this work was carried out in the Characterization Facility, College of Science and Engineering, University of Minnesota, which receives support from the National Science Foundation through the MRSEC (award number DMR-2011401) and the NNCI (Award Number ECCS-2025124) programs.

CONFLICT OF INTEREST

On behalf of all authors, the corresponding author states that there is no conflict of interest.

REFERENCES

1. P. Marcus, *Corros. Sci.* 36, 2155 (1994).
2. B. Gleeson, *Shreirs Corros* (Elsevier, Netherlands, 2010), pp180–194.
3. J.A. Goebel, F.S. Pettit, and G.W. Goward, *Metall. Trans.* 4, 261 (1973).
4. J.A. Goebel and F.S. Pettit, *Metall. Trans.* 1, 3421 (1970).
5. G.W. Goward, *J. Eng. Gas Turbines Power* 108, 421 (1986).
6. N. Eliaz, G. Shemesh, and R.M. Latanision, *Eng. Fail. Anal.* 9, 31 (2002).
7. J. Stringer, *Annu. Rev. Mater. Sci.* 7, 477 (1977).
8. J.M. Alvarado-Orozco, J.E. Garcia-Herrera, B. Gleeson, F.S. Pettit, and G.H. Meier, *Oxid. Met.* 90, 527 (2018).
9. R.A. Rapp, *Corros. Sci.* 44, 209 (2002).
10. K.L. Luthra, *Metall. Trans. A* 13, 1853 (1982).
11. K.L. Luthra and D.A. Shores, *J. Electrochem. Soc. Electrochem. Soc.* 127, 2202 (1980).
12. R.L. Jones, in *High Temp. Corros. Proc. Int. Conf., San Diego, CA, 2–6 Mar, 1981* (1981).
13. I. Gurrappa, I.V.S. Yashwanth, I. Mounika, H. Murakami, and S. Kuroda, *Gas Turbines Mater. Model. Perform.* 1, 55 (2015).
14. I. Gurrappa, *Surf. Coat. Technol.* 139, 272 (2001).
15. B.S. Lutz, J.M. Alvarado-Orozco, L. Garcia-Fresnillo, and G.H. Meier, *Oxid. Met.* 88, 599 (2017).
16. G.H. Meier, *Oxid. Met.* 98, 1 (2022).
17. F. Pettit, *Oxid. Met.* 76, 1 (2011).
18. R.A. Rapp and N. Otsuka, *ECS Trans.* 16, 271 (2009).
19. P.A. Bergman, *Corrosion* 23, 72 (2013).
20. T. Gheno and B. Gleeson, *Oxid. Met.* 86, 385 (2016).
21. D.A. Shifler, *J. Eng. Gas Turbines Power*. <https://doi.org/10.1115/1.4038037> (2017).
22. D.A. Shifler, in *Turbo Expo Power Land Sea Air* (American Society of Mechanical Engineers Digital Collection, 2019), V001T25A001.
23. D.A. Shifler, *Mater. High Temp.* 35, 225 (2018).
24. K.J. Meisner and E.J. Opila, *Oxid. Met.* 94, 301 (2020).
25. J.L. Smialek, F.A. Archer, and R.G. Garlick, *JOM* 46, 39 (1994).
26. T. Gheno and B. Gleeson, *Oxid. Met.* 87, 249 (2017).
27. D.L. Poerschke, R.W. Jackson, and C.G. Levi, *Annu. Rev. Mater. Res.* 47, 297 (2017).
28. C.G. Levi, J.W. Hutchinson, M.-H. Vidal-Sétif, and C.A. Johnson, *MRS Bull.* 37, 932 (2012).
29. E.M. Levin, C.M. Robbins, and H.F. McMurdie, *Phase Diagrams for Ceramics* (1969).
30. B. Hallstedt, *J. Am. Ceram. Soc.* 73, 15 (1990).
31. N. Angelescu and C. Ionita, *Metall. New Mater. Res.* 19, 11 (2011).

32. T. Gheno, G.H. Meier, and B. Gleeson, *Oxid. Met.. Met.* 84, 185 (2015).
33. W. Li and X. Xue, *Process. Saf. Environ. Prot.Saf. Environ. Prot.* 122, 131 (2019).
34. K.Y. Jung, F.S. Pettit, and G.H. Meier, *Materials Science Forum* (Trans Tech Publ, 2008), pp805–812.
35. M.B. Krisak, B.I. Bentley, A.W. Phelps, T.C. Radsick, and J. Propuls, *Power* 33, 697 (2017).
36. P. Brennan, Environmental factors affecting CaO-and CaSO₄-induced degradation of second-generation nickel-based superalloys, PhD Thesis, University of Pittsburgh (2020).
37. M. Kovalchuk and B. Gleeson, in *Superalloys 2020*, ed. by S. Tin, M. Hardy, J. Clews, J. Cormier, Q. Feng, J. Marcin, C. O'Brien, and A. Suzuki (Springer International Publishing, Cham, 2020), pp. 789–797.
38. A.S. Chikhalikar and D.L. Poerschke, *High Temp. Corros. Mater.* 100, 321 (2023).
39. A.S. Chikhalikar, E.P. Godbole, and D.L. Poerschke, *Corros. Sci.. Sci.* 211, 110892 (2022).
40. A.S. Chikhalikar, E.P. Godbole, and D.L. Poerschke, *Acta Mater. Mater.* 237, 118184 (2022).
41. D.W. Green and R.H. Perry, *Perry's Chemical Engineers' Handbook* (McGraw-Hill Education, New York, 2008).
42. N. Kanari, N.-E. Menad, E. Ostrosi, S. Shallari, F. Diot, E. Allain, and J. Yvon, *Metals* 8, 1084 (2018).
43. P.G. Coombs and Z.A. Munir, *J. Therm. Anal.* 35, 967 (1989).
44. D.J. Young, A. Chyrkin, J. He, D. Grüner, and W.J. Quakkers, *Oxid. Met.. Met.* 79, 405 (2013).
45. Y. Wang, Y. Liu, H. Tang, and W. Li, *Mater Charact* 107, 283 (2015).
46. V.K. Tolpygo and D.R. Clarke, *Surf. Coat. Technol.* 120, 1 (1999).
47. V.K. Tolpygo and D.R. Clarke, *Mater. High Temp.* 17, 59 (2000).
48. R. Benrabaa, A. Barama, H. Boukhlouf, J. Guerrero-Caballero, A. Rubbens, E. Bordes-Richard, A. Löfberg, and R.-N. Vannier, *Int. J. Hydrog. Energy* 42, 12989 (2017).
49. R. López-Fonseca, C. Jiménez-González, B. de Rivas, and J.I. Gutiérrez-Ortiz, *Appl. Catal. Gen. Catal. Gen.* 437, 53 (2012).
50. Z. Wang, S.K. Saxena, P. Lazor, and H.S.C. O'Neill, *J. Phys. Chem. Solids* 64, 425 (2003).
51. P. Joshi, P. Saxena, P. Choudhary, M.D. Varshney, and A. Mishra, in *AIP Conf. Proc.* (AIP Publishing LLC, Melville, 2019), p. 020174.
52. H. Du, *J. Phase Equilibria* 21, 6 (2000).
53. Y.M. Lee and C.L. Nassaralla, *Mater. Sci. Eng. A* 437, 334 (2006).
54. P.T. Brennan, D. Konitzer, M. Brennan, and B. Gleeson, *Oxid. Met.. Met.* 98, 43 (2022).
55. G.G. Mikhailov, L.A. Makrovets, and O.V. Samoilova, *Materials Science Forum* (Trans Tech Publ, Switzerland, 2020), pp204–209.
56. C. Greskovich and V.S. Stubican, *J. Phys. Chem. Solids* 30, 909 (1969).
57. R. Sarkar, *Refractory Technology: Fundamentals and Applications* (CRC Press, Florida, 2016), pp113–130.

Publisher's Note Springer Nature remains neutral with regard to jurisdictional claims in published maps and institutional affiliations.

Springer Nature or its licensor (e.g. a society or other partner) holds exclusive rights to this article under a publishing agreement with the author(s) or other rightsholder(s); author self-archiving of the accepted manuscript version of this article is solely governed by the terms of such publishing agreement and applicable law.